nature energy

Article

https://doi.org/10.1038/s41560-023-01418-1

Direct conversion of CO and H_2O to hydrocarbons at atmospheric pressure using a TiO_{2-x}/Ni photothermal catalyst

Received: 23 November 2022

Accepted: 16 November 2023

Published online: 05 January 2024

Check for updates

Xuetao Qin[1,8], Ming Xu[1,2,8], Jianxin Guan[1,8], Li Feng[3,4,8], Yao Xu[1], Lirong Zheng[5], Meng Wang[1], Jian-Wen Zhao[3,4], Jia-Lan Chen[3,4], Jie Zhang[1], Jinglin Xie[1], Zhihao Yu[1], Ruiqi Zhang[1], Xinmao Li[1], Xi Liu[6,7] ✉, Jin-Xun Liu[3,4] ✉, Junrong Zheng[1] ✉ & Ding Ma[1] ✉

Hydrocarbon fuels can be synthesized from CO and water via Kölbel–Engelhardt synthesis, a thermocatalytic process in which temperatures of ≥200 °C and elevated pressures are typically needed. While light-driven hydrocarbon production by CO hydrogenation has been demonstrated under milder conditions, for this reaction H_2 must first be sourced. Here we report the direct production of hydrocarbons from CO and water at atmospheric pressure via light-driven Kölbel–Engelhardt synthesis without external heating or the addition of H_2. Using a TiO_2-supported Ni catalyst, we obtain an activity of 8.83 mol_{-CH2-} mol_{Ni}^{-1} h^{-1} and C_{2+} selectivity higher than 55%. In situ spectroscopy and density functional theory calculations suggest that the migration of photogenerated electrons from TiO_2 to Ni facilitates carbon–carbon coupling at the interface of the TiO_{2-x}/Ni catalyst, which accounts for the observed high selectivity towards multi-carbon products.

The desire to produce valuable hydrocarbons from waste carbon resources and biomass has renewed interest in catalytic CO hydrogenation to liquid fuels, which is also known as Fischer–Tropsch synthesis (FTS)[1,2]. For example, a billion tons of waste CO is produced in industry each year, while the fate of these waste carbon resources is mostly being burned off into CO_2 and/or directly released into the environment[3,4]. Using these waste CO resources to produce high-value-added chemicals or liquid fuels may have advantages in cost, and moreover, making use of waste carbon resources could be a powerful route to mitigate carbon emissions.

Hydrogen at a certain H_2/CO ratio is required to accomplish the FTS process[5,6]. To diminish the usage of hydrogen gas directly, it was proposed by Kölbel and Engelhardt in the 1950s that it is possible to produce hydrocarbons by using CO and H_2O as feeds in a process called Kölbel–Engelhardt synthesis (KES)[7], which integrated the water–gas shift (WGS)[8–11] and CO hydrogenation reactions in the same catalytic system. However, catalysts at the time had very poor catalytic performance, and with the steady supply of petroleum later, interest in this direction faded away[12–14]. Recently, an efficient tandem thermocatalyst, Pt–Mo_2C/C (for WGS reaction) + Ru/C (for FTS process), was reported, which enables the direct conversion of CO and H_2O in the aqueous phase to liquid hydrocarbons[14]. However, the process is limited by the requirement for high-cost noble metal catalysts, and moreover, harsh reaction conditions, such

[1]Beijing National Laboratory for Molecular Engineering, New Cornerstone Science Laboratory, College of Chemistry and Molecular Engineering, Peking University, Beijing, People's Republic of China. [2]State Key Laboratory of Chemical Resource Engineering, Beijing University of Chemical Technology, Beijing, People's Republic of China. [3]Department of Chemical Physics, University of Science and Technology of China, Hefei, People's Republic of China. [4]Hefei National Laboratory, University of Science and Technology of China, Hefei, China. [5]Institute of High Energy Physics, The Chinese Academy of Sciences, Beijing, People's Republic of China. [6]School of Chemistry and Chemical Engineering, In-situ Center for Physical Sciences, Shanghai Jiaotong University, Shanghai, People's Republic of China. [7]Syncat@Beijing, Synfuels China Co., Ltd, Beijing, People's Republic of China. [8]These authors contributed equally: Xuetao Qin, Ming Xu, Jianxin Guan, Li Feng. ✉e-mail: liuxi@sjtu.edu.cn; jxliu86@ustc.edu.cn; junrong@pku.edu.cn; dma@pku.edu.cn

https://doi.org/10.1038/s41560-023-01418-1

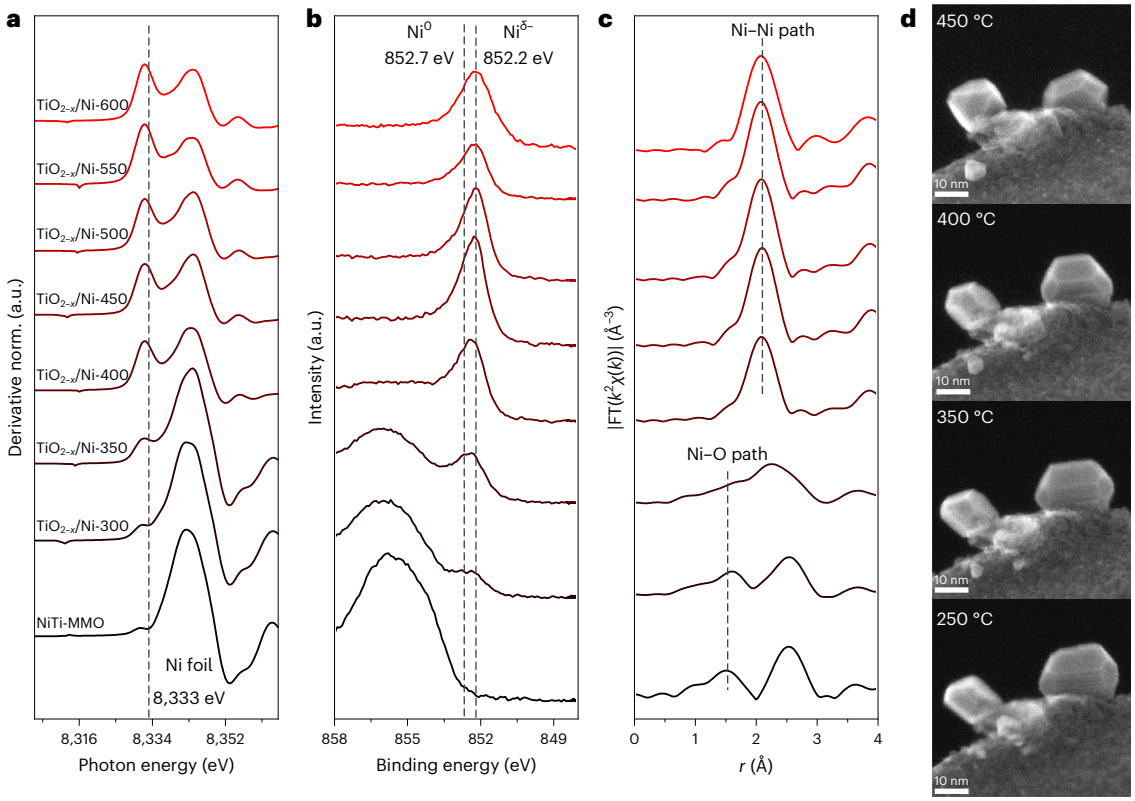

Fig. 1 | Characterization results of the catalyst structure. a, The first derivative spectra of Ni K-edge XANES of Ni-TiMMO and TiO_{2-x}/Ni-*T*. Derivative norm. is the notation for the normalized intensity of the first derivative signal. **b**, Quasi in situ XPS spectra of Ni $2p_{3/2}$ for Ni-TiMMO and TiO_{2-x}/Ni-*T*. **c**, The Fourier transform (FT) of the EXAFS spectra of Ni-TiMMO and TiO_{2-x}/Ni-*T*. **d**, In situ STEM images of the TiO_{2-x}/Ni catalyst after reduction in a H_2 atmosphere (10 Pa) at 250 °C, 350 °C, 400 °C and 450 °C.

as a high reaction pressure (at least 3 MPa), impose a high energy requirement. Therefore, it is highly desirable to develop the catalytic system driven by renewable energy to convert CO and H_2O into hydrocarbons, which can operate under mild reaction conditions, that is, at atmospheric pressure and using earth-abundant transition metals as catalysts. It has been reported that, under light irradiation, CO can react with H_2O for WGS reaction and CO can be hydrogenated by molecular H_2 into methane and other hydrocarbons[15–19]. However, the processes of CO hydrogenation reactions require the use of high-pressure hydrogen, and a specific H_2:CO ratio is needed to successfully convert CO (refs. 15,16).

In this article, we report a direct synthesis of hydrocarbons from CO and H_2O via photo-driven catalysis under atmospheric pressure, and no extra heating is needed. TiO_2-supported earth-abundant nickel catalysts were demonstrated to be able to convert CO and water into hydrocarbons under photo-irradiation. The space–time yield of hydrocarbons obtained over TiO_{2-x}/Ni-450 catalyst is as high as 8.83 mol_{-CH2-} mol_{Ni}^{-1} h^{-1}. The photo-driven catalytic reaction was studied using a combination of various in situ techniques. The integrated spectroscopic evidence shows that, in addition to providing the heat required for the reaction, the light facilitates charge transfer from TiO_{2-x} to Ni and consequently shifts CO hydrogenation towards C_{2+} over the TiO_{2-x}/Ni interface in photothermal synthesis. Density functional theory (DFT) calculations indicate that the presence of the photon-induced electron accelerates the CH–CH coupling process and improves the CH surface coverage, which promotes the selectivity to C_{2+} products compared with the thermocatalytic reaction. We have confirmed the possibility of using water as the hydrogen donor to accomplish photo-driven CO conversion to hydrocarbons under atmospheric pressure.

The structure of the photothermal catalyst

The NiTi-layered double hydroxides (LDH) nanosheets were synthesized by a hydrothermal method[10,20]. Mixed oxides (NiTi-MMO) composed of NiO and TiO_{2-x} were fabricated by calcining NiTi-LDHs at 500 °C for 4 h (Supplementary Fig. 1). Quasi in situ X-ray diffraction (XRD), X-ray absorption spectroscopy (XAS), ultraviolet–visible–near infrared (UV–Vis–NIR) spectrophotometry and X-ray photoelectron spectroscopy (XPS) were used to analyse the structure of TiO_{2-x}/Ni catalysts reduced at various temperatures (*T* indicates the reduction temperature of catalysts, denoted TiO_{2-x}/Ni-*T*). The Ni species were reduced to the metallic state at 400 °C (Fig. 1a–c and Supplementary Figs. 2 and 3). At 450 °C, the Ni absorption edge of the TiO_{2-x}/Ni-450 catalyst shifted to lower energy than that of Ni foil, indicating the presence of $Ni^{\delta-}$ species with lower valence than the metallic state. The absorption edge and its first derivative gradually migrate to lower energy as the reduction temperature rises (Fig. 1a and Supplementary Fig. 3). From the quasi in situ XPS results (Fig. 1b), the peak attributed to nickel oxide dominates the $2p_{3/2}$ spectra at reduction temperatures lower than 350 °C, while peaks at 852.7 and 852.2 eV become the main peaks at 350 °C or higher, which is due to the presence of Ni^0 and $Ni^{\delta-}$ species, respectively. Even at high reduction temperatures, the peak at 852.2 eV becomes the majority of the spectrum, indicating that a larger proportion of $Ni^{\delta-}$ species formed in the further reduced catalyst. Previously, it was reported that the strong metal–support interaction (SMSI) between Ni and TiO_{2-x} will enable electron transfer from the TiO_{2-x} support to the Ni species, which accounts for the observed electronic character of $Ni^{\delta-}$ species[20].

The diffuse reflectance UV–Vis–NIR spectra of TiO_{2-x}/Ni-*T* (Supplementary Fig. 4) were used to investigate the light absorption behaviour of the catalysts. In contrast to Ni-TiMMO, which shows

https://doi.org/10.1038/s41560-023-01418-1

Table 1 | Photothermal catalytic performance of Ni-based catalysts[a]

Entry	Photocatalyst	CO conversion (%)	Hydrocarbon selectivity (%)			WGS activity (mol CO_2 mol_{Ni}^{-1} h^{-1})	FTS activity (mol_{-CH2-} mol_{Ni}^{-1} h^{-1})	Activity (mol CO mol Ni^{-1} h^{-1})
			CH_4	C_2–C_4	C_{5+}			
1	Blank[b]	0	–	–	–	–	–	–
2	TiO_{2-x}/Ni-300	9.8	70.5	26.5	3.0	3.33	0.62	5.00
3	TiO_{2-x}/Ni-350	14.8	52.8	36.2	11.0	5.91	1.28	8.24
4	TiO_{2-x}/Ni-400	31.9	51.1	37.0	11.9	16.47	3.29	21.89
5	TiO_{2-x}/Ni-450	34.8	44.3	44.9	10.8	20.41	5.04	26.90
6	TiO_{2-x}/Ni-500	26.5	41.2	48.2	10.6	15.54	4.05	20.74
7	TiO_{2-x}/Ni-550	15.7	38.2	51.0	7.8	7.94	1.77	11.13
8	TiO_{2-x}/Ni-600	12.42	36.7	57.0	6.3	6.72	1.49	9.77
9	TiO_{2-x}/Ni-450[c]	12.1	44.5	45.6	9.9	35.61	8.83	46.76
10	TiO_{2-x}/Ni-450[d]	8.1	48.1	41.7	10.2	4.16	0.97	6.26

[a]Reaction conditions: no external heating, irradiation time: 120 min, 300 W Xe lamp (200–1,000 nm), light intensity: 1.53 W cm^{-2} (apparent temperature of the catalyst bed: 220 °C), CO/Ar = 96/4, 100 µl H_2O, catalyst mass: 50 mg. The activity was normalized over surface Ni according to CO chemisorption results. [b]Blank experiment: irradiation in the absence of any catalyst in CO and H_2O or illumination of the catalysts in Ar under above conditions. [c]Catalyst mass: 10 mg. [d]Simulated sunlight experiment: under the same experimental conditions with a solar simulator instead of the Xe lamp, apparent temperature of the catalyst bed: 54 °C.

a strong absorption primarily in the UV region, TiO_{2-x}/Ni-*T* exhibits a broad absorption across the entire spectrum, indicating the full-spectrum-absorption ability of TiO_{2-x}/Ni-*T*. The apparent temperature of the TiO_{2-x}/Ni-450 catalyst bed ranges from 202 °C to 248 °C under different light intensities (shown in Supplementary Fig. 10a). Interestingly, the in situ XPS spectra of the Ni 2*p* shell of the TiO_{2-x}/Ni-450 catalyst (Supplementary Fig. 5) show that, under light-on and light-off conditions in sequence, the Ni $2p_{3/2}$ peak shifted to an even lower binding energy under the re-irradiation conditions and subsequently returned to the original position under the light-off condition, which demonstrates the reversible charge accumulation on the Ni surface induced by light irradiation. This means that the Ni species may serve as a charge acceptor/donor during the photocatalytic process.

Environmental STEM with an secondary electron detector is used to demonstrate the inherent physicochemical behaviour of Ni-based catalysts. In particular, the surface morphology of TiO_{2-x}/Ni catalysts can be explored under working conditions. The passivated TiO_{2-x}/Ni-*T* catalysts were reduced in a H_2 atmosphere (pressure 10 Pa) at different reduced temperatures for 1 h. The morphology of the Ni nanoparticles gradually changes into regular truncated octahedrons as the reduction temperature increases from 250 °C to 450 °C, and the Ni nanoparticles are embedded into TiO_{2-x} (or the migration of TiO_{2-x} onto Ni nanoparticles) at the same time (Fig. 1d and Supplementary Figs. 6 and 7). The strong interaction between Ni nanoparticles and TiO_{2-x} can be adequately illustrated by the above-verified results.

Photothermal catalytic performance

We then evaluated the catalytic performance of TiO_{2-x}/Ni catalysts for CO and H_2O conversion under light irradiation at atmospheric pressure. The results are summarized in Table 1 and Supplementary Table 2. Light irradiation without the catalyst gives no products (Table 1, entry 1). Additionally, the oxide precursor (NiTi-MMO) displays a poor CO conversion (1.7%; Supplementary Table 2, entry 1). In contrast, the reduced catalysts display considerable activity, and a strong dependence of activities on the reduction temperature can be observed as well. A key role of WGS in photothermal catalysis is evidenced by the appreciable production of CO_2 and H_2 in all the reduced catalysts, but activities for subsequent CO hydrogenation emerged and increased with the reduction of Ni. TiO_{2-x}/Ni-300, with a lower content of metallic Ni species, exhibits a CO conversion of 9.8% with methane as a major product in hydrocarbons (Table 1, entry 2). Both the CO conversion and C_{2+} selectivity gradually increased as the reduction temperature increased from 300 °C to 450 °C (Table 1, entries 2–5), and later, the C_{2+} selectivity exceeded the selectivity to methane, indicating that the metallic Ni species or even the $Ni^{\delta-}$ species are the active sites for the photo-driven cascade KES reaction[21–23]. The CO conversion reached a maximum and dropped afterwards when the reduction temperature rose from 450 °C to 600 °C, which should be due to the decrease in the number of exposed Ni sites and possibly further changes in the electronic structure of Ni species after reduction at high temperatures (Table 1, entries 5–8 and Supplementary Fig. 12). In the environmental STEM experiments, we observed that TiO_{2-x} migrated obviously to Ni nanoparticles and even coated Ni nanoparticles to a certain extent when the reduction temperature reached 600 °C (Supplementary Figs. 17 and 18) due to the strong interaction, which is consistent with the CO chemisorption results (Supplementary Figs. 8 and 9 and Supplementary Table 1). This could explain why the activity of catalysts declines when the reduction temperature exceeds 450 °C.

In contrast, the Ni/Al_2O_3 catalyst is unable to catalyse the formation of hydrocarbons under irradiation but exhibits activity to WGS (Supplementary Table 6, entry 3) with a CO conversion of less than 10% and the major product being CO_2. This suggests that the TiO_{2-x}/Ni catalysts formed under SMSI, not solo metallic Ni, are pivotal in photo-driven CO and H_2O to hydrocarbon reaction, while the unique structure of TiO_{2-x}/Ni confers the catalyst the ability to absorb the light and finish the chemical transformation.

The experiment utilizes the ^{13}CO as feed during the photothermal catalytic KES reaction to trace where carbon goes. The carbon source of the hydrocarbons is CO as confirmed by isotopic labelling experiments (Supplementary Fig. 14). The selectivity for hydrocarbon products obtained from the TiO_{2-x}/Ni catalyst follows the Anderson–Schulz–Flory distribution (Supplementary Fig. 15), with a relatively small growth factor (α) of 0.447.

After optimization of the reaction conditions (Supplementary Tables 3–5), the TiO_{2-x}/Ni-450 catalyst achieved a hydrocarbon formation activity of 8.83 mol_{-CH2-} mol_{Ni}^{-1} h^{-1} and C_{2+} selectivity of 55.5% under irradiation (Table 1, entry 9), which even overwhelmed the performance of thermal catalytic KES reactions reported in the literature (Supplementary Table 7). More interestingly, the TiO_{2-x}/Ni-450 catalyst is also active under simulated sunlight (Table 1, entry 10). The conversion of CO was 8.1% in 2 h, while the selectivity of C_{2+} hydrocarbons was over 51.9%. The TiO_{2-x}/Ni-450 catalyst also shows good stability, and the

https://doi.org/10.1038/s41560-023-01418-1

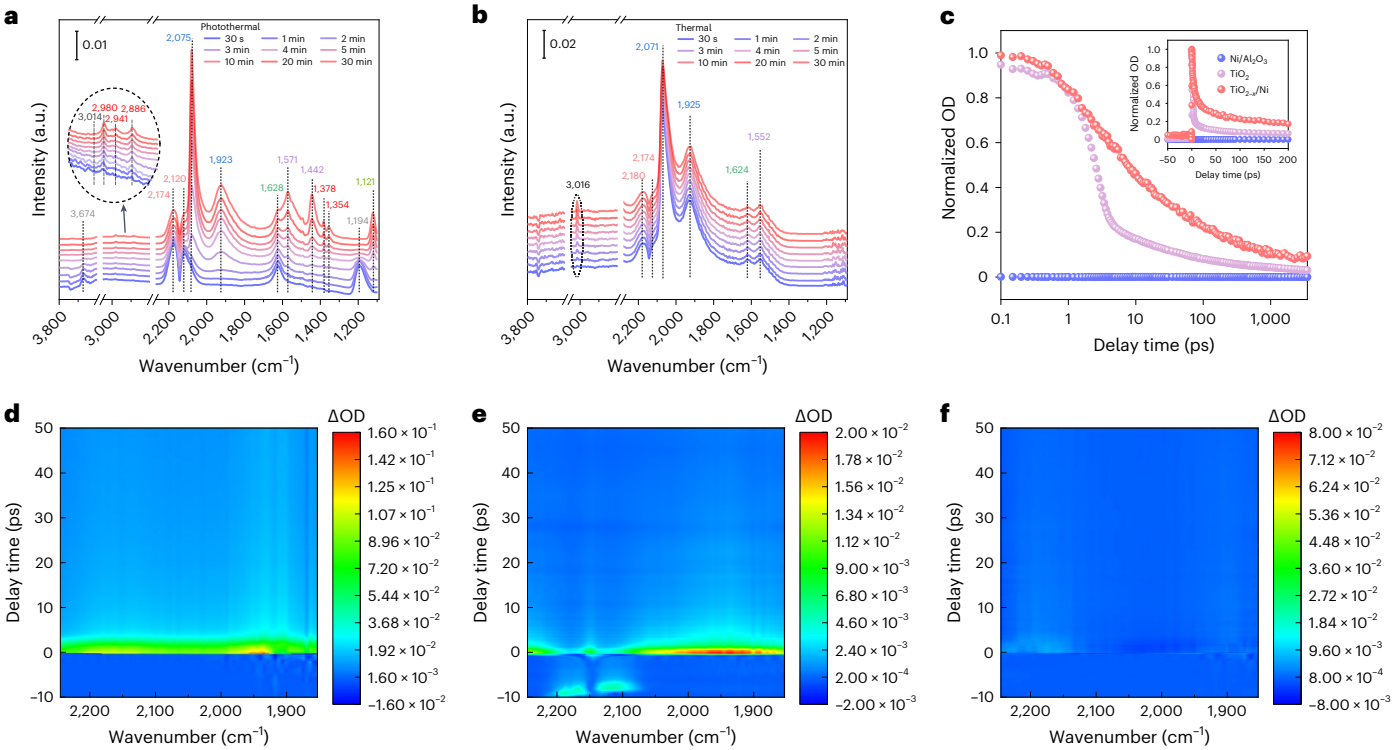

Fig. 2 | Probing the mechanism of the photothermal catalytic reaction by in situ DRIFTS and in situ ultrafast IR spectroscopy. a,**b**, In situ time-resolved DRIFTS was carried out over the TiO_{2-x}/Ni-450 catalyst under Xe lamp irradiation (**a**) and at 220 °C without irradiation (**b**). **c**, Signal decays of TiO_{2-x}/Ni-450, Ni/Al_2O_3 and TiO_2 detected in the in situ reaction at 2,073 cm^{-1}. **d**–**f**, In situ ultrafast Vis pump/IR probe spectra of TiO_2 (**d**), TiO_{2-x}/Ni-450 (**e**) and Ni/Al_2O_3 (**f**) at waiting times of −20 ps to 50 ps at 2,245–1,853 cm^{-1}, respectively. OD, optical density.

structure of the catalyst remains almost unchanged according to in situ XAS and in situ XPS (Supplementary Fig. 16).

We also evaluated the contribution of heat to the catalytic activity. We noticed that the temperature of the catalyst bed increased rapidly during the first 5 min of irradiation and then stabilized at 202–248 °C after 30 min (Supplementary Fig. 10a). A control reaction was carried out at the same temperature without light irradiation to check the impact of light on the reaction. Only 10.8% of CO was converted after 2 h of reaction at 220 °C (Supplementary Fig. 13), and the WGS product, CO_2, was the major product, which again indicates the importance of the photo-irradiation in current process (Supplementary Table 6, entry 1). Therefore, it seems that the formation of hydrocarbons is unlikely to be accomplished from the thermal energy generated from irradiation, while the C–C coupling step on TiO_{2-x}/Ni is most likely a photon-driving process.

Investigating the photothermal catalytic reaction mechanism

So far, limited by the complex reaction system and the difficulty in clarifying the role of photons, the mechanism of most photothermal catalytic processes remains ambiguous. This problem has been investigated by using in situ spectroscopic experiments[24]. During photocatalytic or photothermal catalytic reactions, academics have paid extensive attention to the electron transfer process once the catalyst material is activated by photons[25]. However, the direct observation of electron migration in the catalyst during the photothermal process is still not achieved. To further understand the mechanism of photocatalytic or photothermal catalytic reaction processes, in situ characterization with ultrafast response is urgently needed. In situ time-resolved diffuse reflectance Fourier transform spectroscopy (DRIFTS) was carried out in this work to investigate the reaction routes in terms of activation of CO and formation of intermediates (Fig. 2a,b). More crucially, we used in situ ultrafast IR spectroscopy (Fig. 2c–f) to identify short-lived transient species over various catalysts and distinguish their photocatalytic behaviours associated with photon excitation, which could help us better understand the difference between photocatalysis and photothermal catalysis.

The IR bands at ~2,075/2,071 cm^{-1} and ~1,925/1,923 cm^{-1} in Fig. 2a,b, which are assigned to linear adsorbed CO species on Ni defect sites and bridge adsorbed species on $Ni^{\delta-}$ sites, respectively, are both observed under photothermal or thermal conditions after CO and H_2O adsorption (Supplementary Fig. 19)[10,20]. The IR bands at ~2,941 cm^{-1} (asymmetric υ_{as}(C–H) stretching vibrations of CH_x* species) and ~2,886 cm^{-1} (symmetric υ_s(C–H) stretching vibrations of CH_x* species) and the IR bands at ~1,378 cm^{-1} and ~1,354 cm^{-1} corresponding to the bending vibrations of CH_x* species gradually increase with increasing irradiation time (Fig. 2a)[26]. In addition, no notable IR band at 3,016 cm^{-1} (assigned to the υ(C–H) stretching vibration of CH_4 molecules) can be identified[27,28]. This shows that C_{2+} hydrocarbon compounds, rather than CH_4, are the major products of photothermal catalysis. Meanwhile, no infrared vibrations of CH_x* species were observed in the thermal catalytic experiment, but there was a strong υ(C–H) stretching vibration of CH_4 at 3,016 cm^{-1}, indicating that methane was the major product of hydrocarbons in the thermal catalytic process. This is also consistent with our activity results (Supplementary Table 6 and Supplementary Fig. 13). Surprisingly, we found the presence of exceptional reaction intermediates (1,600 cm^{-1} to 1,100 cm^{-1} belonged to C–O and C–C vibrations) under photothermal conditions in contrast to the thermal conditions, in addition to product changes, which demonstrates that the photocatalytic process could alter the conventional chemical route, allowing for more hydrocarbon compounds to be produced.

Moreover, in situ ultrafast Vis pump/IR probe spectroscopy was carried out to study such a photon-induced electron excitation and transfer process, which expectedly played a vital role in the

https://doi.org/10.1038/s41560-023-01418-1

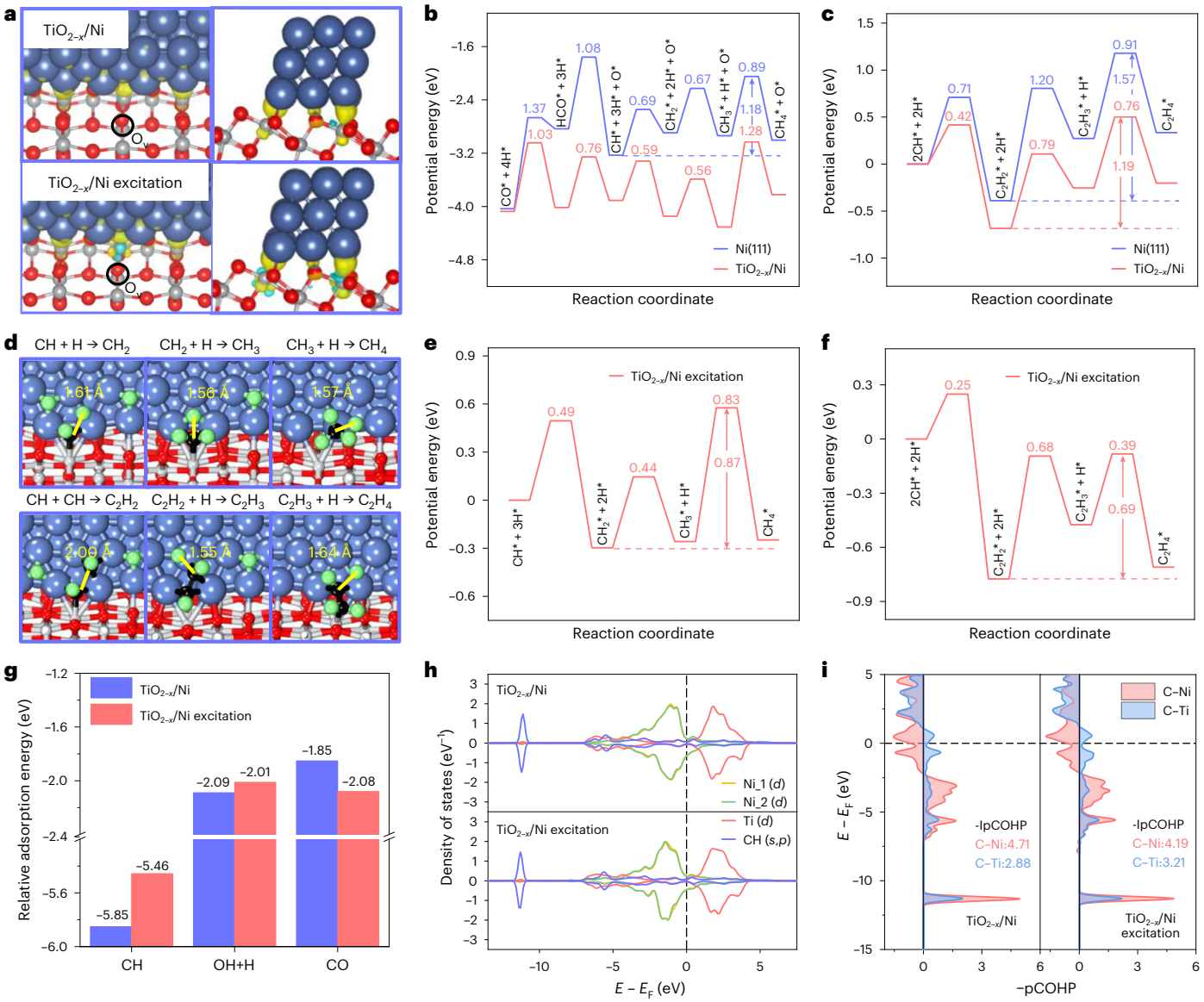

Fig. 3 | DFT studies on the mechanism of CO hydrogenation. a, Top and side views of isosurfaces of the differential charge density of the Ni ribbon adsorbed on the TiO_{2-x}/Ni and photo-excited TiO_{2-x}/Ni surface with isovalues of 0.007 |e| $Å^{-3}$. Yellow and cyan colours represent charge depletion and accumulation, respectively. **b**, Potential energy diagram for CO methanation over Ni(111) and TiO_{2-x}/Ni surfaces. **c**, Potential energy diagram for C_2H_4 formation via CH–CH coupling over Ni(111) and TiO_{2-x}/Ni surfaces. The forward activation barriers are indicated in eV. **d**, Key transition state configurations for CH_4 and C_2H_4 formation at the interface of photo-excited TiO_{2-x}/Ni(111) surface. The bond distances between two fragments at the transition states are indicated in Å. The blue, grey, red/green and black spheres are Ni, Ti, O and C atoms, respectively. **e**,**f**, Potential energy diagrams for CH_4 (**e**) and C_2H_4 (**f**) formation over the photo-excited TiO_{2-x}/Ni surface, respectively. **g**, Comparisons of the adsorption energies of CH, OH/H and CO over the TiO_{2-x}/Ni and photo-excited TiO_{2-x}/Ni surfaces. **h**,**i**, Density of state (DOS) (**h**) and the projected crystal orbital Hamilton population (pCOHP) plots (**i**) of C–Ni/C–Ti bonds for CH adsorption at the interface of TiO_{2-x}/Ni and photo-excited TiO_{2-x}/Ni surfaces, respectively.

photothermal reaction. Upon excitation, broad band absorption appears, reaches maxima almost instantaneously and diminishes quickly, ranging from 1,300 cm^{-1} to 3,000 cm^{-1} (Fig. 2e and Supplementary Figs. 21 and 22), which is attributed to the generation of a larger quantity of free electrons[29–33] (Supplementary Figs. 20 and 23). The pure TiO_2 illustrates representative cooling and trapping processes (Fig. 2d), whereas Ni/Al_2O_3 shows a tiny signal and fast-decaying process of free electrons (Fig. 2f), indicating that free electron excitation originates from TiO_2 instead of Ni upon 520 nm excitation. Compared with Ni/Al_2O_3 and TiO_2, the TiO_{2-x}/Ni-450 catalyst shows a notably longer relaxation process (Fig. 2c–f), which indicates that the electron transfer process occurs from TiO_{2-x} to Ni, leading to a much more difficult trapping process in TiO_{2-x}. In the photon-induced electron excitation and relaxation process of the TiO_{2-x}/Ni-450 catalyst (Fig. 2e), two absorption peaks at ~2,170 cm^{-1} and ~2,120 cm^{-1} appear upon 520 nm excitation, which are assigned to the excited state absorptions of CO located on different sites on Ni. These two peaks slightly redshift induced by the electronic excitation compared with their respective peaks of the ground state absorptions located at 2,174 cm^{-1} and 2,120 cm^{-1} in the Fourier-transform IR spectrum (Fig. 2a), suggesting that free electrons transfer to CO, which is also supported by our DFT calculations. The emergence of the CO vibrational relaxation on Ni active sites implies that free electrons transfer from metallic Ni to CO after the electron transfer process occurring from TiO_{2-x} to Ni under irradiation. Therefore, we conclude that the free electron excitation probably originates from TiO_2 and then transfers to Ni and eventually to CO.

Reaction mechanism identification by DFT calculations

DFT calculations were performed to understand the CO hydrogenation mechanism over the TiO_{2-x}/Ni catalyst, where Ni nanocrystals are supported on a partially reduced TiO_2 substrate. The interfacial TiO_{2-x}/Ni catalyst was modelled by using a three-layered Ni ribbon consisting of three columns of Ni atoms adsorbed on oxygen-deficient TiO_2(101) (Fig. 3a). The Ni(111) surface was first studied as a reference because it is uniformly exposed on the metallic Ni nanoparticle (Fig. 1d). During the photo-driven thermal catalysis, the most favourable hydrogen-assisted CO activation via HCO in the formation of CH monomers (Fig. 3b and Supplementary Figs. 24, 25, 31 and 32) is identified as the rate-determining step for CO methanation over the Ni(111) surface with an overall activation barrier of 2.27 eV (Fig. 3b). Although the hydrogenation of the CH monomer and the most likely CH–CH coupling (Supplementary Table 8) has similar activation barriers (0.69 eV versus 0.71 eV), subsequent hydrogenation of CH_2 towards CH_4 is preferable to the hydrogenation of C_2H_2 toward C_2H_4 by 0.39 eV due to the higher endothermic reaction energy for the latter reaction over the Ni(111) surface (Fig. 3b,c and Supplementary Figs. 31 and 32). Our calculation results are corroborated by our experimental measurements that CH_4 is the major product for CO hydrogenation over Ni/Al_2O_3 via the photo-driven thermal catalytic procedure (Supplementary Table 6).

As compared with Ni(111) surface, the interfacial sites of the TiO_{2-x}/Ni surface improve the energetics of CO hydrogenation. For example, CO activation is enhanced at the interface of the TiO_{2-x}/Ni catalyst in the formation of CH monomer (E_a = 1.03 eV) attributed to the strong attractive interactions between Ti atoms and O atoms in CO/HCO intermediates lowering the transition state energies (Fig. 3b and Supplementary Figs. 24, 25, 33 and 34). The activation barrier for the most favourable CH–CH coupling decreases from 0.71 eV over Ni(111) to 0.42 eV over TiO_{2-x}/Ni (Fig. 3c), which indicates the essential role of the TiO_{2-x}/Ni interface in accelerating carbon–carbon coupling in the formation of long-chain hydrocarbons. Compared with direct CH hydrogenation, CH–CH coupling is easier to take place by 0.17 eV for further hydrogenation (Fig. 3b,c), which principally results in a high selectivity of the C_2 product on the TiO_{2-x}/Ni catalyst via a thermal catalytic procedure[34]. However, the dissociative adsorption of the H_2O reactant (OH/H) suppresses CO adsorption at the interface of the TiO_{2-x}/Ni catalyst by 0.24 eV (Fig. 3g), resulting in a relatively low surface coverage of the CH monomer, which thus gives a low reaction rate of CH–CH coupling[35]. Therefore, CH_4 remains the major product for CO hydrogenation at the interface of TiO_{2-x}/Ni catalysts via photo-driven thermal catalysis (Supplementary Table 6); however, this cannot explain the higher selectivity of C_{2+} found over the TiO_{2-x}/Ni catalysts under light.

An external electron added to the TiO_{2-x}/Ni surface was used to model the photo-excited TiO_{2-x}/Ni catalyst, where the photoinduced electron generated in TiO_{2-x} can be transferred from interfacial Ti to Ni (Fig. 3a), as corroborated by our in situ ultrafast IR spectroscopy experiment (Fig. 2c–f). We found that the presence of an extra electron in the photo-excited TiO_{2-x}/Ni surface promotes CH–CH coupling and direct CH hydrogenation by 0.17 eV and 0.10 eV, respectively (Fig. 3d–f and Supplementary Figs. 35 and 36). The lower activation barriers for CH hydrogenation and CH–CH coupling are attributed to their higher exothermic reaction energies driven by the weaker CH intermediate adsorption by 0.39 eV (Fig. 3g) over the photo-excited TiO_{2-x}/Ni surface. The origin for the weakened CH adsorption comes from the large charge transfer from the photo-excited TiO_{2-x}/Ni surface to the CH monomer and more occupation of the antibonding orbitals of Ni–C bonds (Fig. 3h,i). Similar to the TiO_{2-x}/Ni surface, CH–CH coupling remains more preferable than direct CH hydrogenation by 0.24 eV at the interface of the photo-excited TiO_{2-x}/Ni surface. The presence of an extra electron slightly increases CO adsorption by 0.23 eV, which might be due to the stabilization of the CO adsorbed photo-excited TiO_{2-x}/Ni surface by forming stronger Ti–O bonds by decreasing the bond distances with a maximum of 0.06 Å (Supplementary Figs. 26). As a result, the comparable adsorption energies of H_2O dissociative adsorption (OH/H) and CO adsorption (−2.01 eV versus −2.08 eV; Fig. 3g) gives a relatively high surface coverage of CH_x intermediates for CH–CH coupling promoting C_{2+} production over photo-excited TiO_{2-x}/Ni. One layer Ti_6O_{12} cluster anchored on Ni(111) surface (Supplementary Figs. 27 and 28) was used to model the alternative interface formed by the thin TiO_{2-x} overlayer covering on Ni nanoparticles due to the SMSI effect. Nearly the same results can be found at the interface of Ni/Ti_6O_{11} surface (Supplementary Figs. 27, 28, 37 and 40). The comparable low activation barriers for CH–CH coupling over the TiO_{2-x}/Ni and Ni/Ti_6O_{11} surfaces (0.24 eV versus 0.18 eV) indicate that both interfaces could contribute to the high selectivity of CO hydrogenation towards C_2 over the synthesized catalyst via photothermal catalytic procedure. Therefore, the high selectivity of CO hydrogenation towards C_{2+} could stem from the acceleration of the CH–CH coupling process and the improvement of CH surface coverage at the interface of the TiO_{2-x}/Ni catalyst via photothermal catalysis.

Conclusions

We demonstrated that the TiO_{2-x}/Ni catalyst fabricated from LDHs enables the direct production of hydrocarbons from CO and H_2O under photo-irradiation at atmospheric pressure. The TiO_{2-x}/Ni-450 catalyst has an activity of 8.83 mol_{-CH2-} mol_{Ni}^{-1} h^{-1} and >55% C_{2+} selectivity, which accomplished KES processes efficiently. The photogenerated electron transfer process of the catalyst and the changes in reactant species during the reaction were probed using in situ ultrafast IR and DRIFTS. DFT calculations reveal that the high selectivity of C_{2+} at the interfacial TiO_{2-x}/Ni-450 catalyst might stem from accelerating CH–CH coupling and improving the CH surface coverage during photothermal catalysis. Our work not only establishes a catalyst for the efficient direct conversion of CO and H_2O to hydrocarbons under mild conditions but also offers the approach to investigating the role of light and photogenerated electrons in the photothermal catalytic reaction process.

Methods

Catalyst preparation

First, similar to our earlier work, the ultrathin NiTi-LDH precursor was synthesized using a redesigned hydrothermal synthesis approach[10,20]. $Ni(NO_3)_2{\cdot}6H_2O$ (0.006 mol), HCl (0.25 ml), $TiCl_4$ (0.25 ml) and urea (0.1 mol) were dissolved in de-ionized water (100 ml) under vigorous stirring for 24 h at 95 °C in a typical method. The resultant solid was centrifuged, thoroughly washed and dried overnight at 60 °C. After that, NiTi-LDH nanoplates were calcined in a muffle furnace under air at 500 °C for 4 h with a heating rate of 2 °C min^{-1} to obtain mixed oxide NiTi-MMO (a mixture of NiO and TiO_2). Next, the as-obtained NiTi-MMO mixed oxides were reduced in a H_2/Ar (10:90, v/v) stream for 4 h at different temperatures, such as 300, 350, 400, 450, 500, 550 and 600 °C, with a flow rate of 60 ml min^{-1} and a heating rate of 2 °C min^{-1}, which were indicated as TiO_{2-x}/Ni-300, TiO_{2-x}/Ni-350, TiO_{2-x}/Ni-400, TiO_{2-x}/Ni-450, TiO_{2-x}/Ni-500, TiO_{2-x}/Ni-550 and TiO_{2-x}/Ni-600, respectively. For comparison, the 15% Ni/Al_2O_3 catalyst was made using the traditional impregnation method. An aqueous solution containing 0.55 mmol $Ni(NO_3)_2{\cdot}6H_2O$ was mixed with the commercial Al_2O_3 support (1 g) in a conventional process. The suspension liquid was stirred for 3 h, and then the suspension liquid was changed into a drying oven at 120 °C overnight. To obtain the 15% Ni/Al_2O_3 catalyst, the as-synthesised material was reduced under 10% H_2/Ar with a flow rate of 60 ml min^{-1} for 4 h at 450 °C (a heating rate of 5 °C min^{-1}).

Characterization of catalysts

Powder XRD. Powder XRD experiments were carried out on an X-Pert[3] Powder diffractometer with Cu Kα radiation (condition: 40 kV, and 100 mA, scan rate of 5° min^{-1}) and a 2θ angle ranging from 5° to 80°. The crystal structures of components could be identified on the basis of the Joint Committee on Powder Diffraction Standards standard cards.

Inductively coupled plasma-atomic emission spectrometer. The actual contents of the supported metals were determined using a Prodigy 7 inductively coupled plasma-atomic emission spectrometer (Leeman). All the samples were dissolved with aqua regia at 100 °C before the test.

CO chemisorption. Ni dispersions were measured by static chemisorption of CO on a Micromeritics ASAP 2020 apparatus at 35 °C. Sample of 0.47 g (20–60 mesh) was loaded in a sample tube. Then the sample was outgassed under vacuum at 200 °C for 6 h and reduced under pure H_2 at different temperatures (that is, 300, 350, 400, 450, 500, 550 and 600 °C) for 4 h. After cooling to 35 °C at vacuum, pure CO was introduced to the system. The first isotherm gives the total amount of adsorbed CO and the second isotherm gives the reversible part of adsorbed CO. The difference between the two isotherms gives the irreversible part of chemisorbed CO. The Ni dispersion was supposed for the adsorption stoichiometry of CO to Ni to be 1 for the TiO_{2-x}/Ni catalyst.

UV–Vis–NIR spectrophotometry. UV–Vis–NIR spectroscopy was performed on a Shimadzu UV3600Plus UV–Vis–NIR spectrophotometer in the Analytic Instrumentation Center of College of Chemistry and Molecular Engineering at Peking University, which was equipped with three detectors: a PMT detector that detects ultraviolet and visible regions, and an InGaAs and PbS detector that detects NIR regions. The absorption spectrum of solid powder samples was tested in the band of 200–2,500 nm, using $BaSO_4$ as the blank control sample.

XPS. XPS measurements were conducted on an Axis Ultra imaging photoelectron spectrometer equipped with an Al Kα quartz monochromator source. Quasi in situ XPS results of the reduced and used catalysts were measured by transferring the samples to the measurement chamber without exposure to air. The binding energy was corrected by setting the active carbon sp^2 C_{1s} of 284.8 eV as the reference. Synchronous illumination XPS was performed by equipping with a 300 W xenon lamp as the illumination source.

XAS. The XAS spectra of the Ni K edge (8,333 eV) were collected at beamline 1W1B of the Beijing Synchrotron Radiation Facility, Institute of High Energy Physics, Chinese Academy of Sciences. The beam was tuned by the Si(111) double-crystal monochromators. The energies were calibrated according to the absorption edge of pure Ni foil. The typical energy of the storage ring was 2.5 GeV with a maximum current of 250 mA. For quasi in situ XAS spectra of the reduced and used catalysts, the powdered sample was pressed into the sheet in the glovebox without exposure to air. For in situ XAS spectra of TiO_{2-x}/Ni-450 under reaction conditions, the NiTi-MMO sample was first pressed into the sheet and loaded into a reactor cell equipped with polyimide windows. The sample sheet was reduced in a H_2/He stream at 450 °C in the reactor cell, followed by flushing (50 ml min^{-1}) with high purity He for 1.0 h, and then 50 ml min^{-1} CO with water vapour flows into the reactor cell under irradiation. The in situ XAS spectra at the Ni K-edge were collected.

Scanning transmission electron microscopy. The sample was directly dispersed in a mems chip used for an in situ environmental scanning transmission electron microscopy (STEM) experiment. After inserting a heating holder equipped with the prepared chip inside the TEM, H_2 gas was introduced into the TEM column, and the pressure was maintained at 2 Pa. The temperature gradually increased from 200 °C to 450 °C. The structural evolution was recorded under STEM mode (Hitachi HF5000 probe-corrected environmental STEM, cold field emission gun, accelerating voltage 200 kV). The instrument enables simultaneous imaging of annular bright-field, annular dark-field and secondary electron images of an identical particle. Electron energy loss spectroscopy was collected by the Gatan 965 energy filter.

DRIFTS. In situ DRIFTS was also carried out to further monitor the dynamic evolution of reactive molecules, active intermediates and products with irradiation or without irradiation for the reaction of CO and H_2O over the TiO_{2-x}/Ni-450 catalyst. For the TiO_{2-x}/Ni-450 catalyst, the powdered sample (NiTi-MMO) was filled into the reactor, prereduced in 10% H_2 (Ar balance) at 450 °C for 4 h and flushed with high-purity Ar for 30 min. Afterwards, the temperature was decreased to 220 °C. Then, CO (CO:Ar = 5:95; 30 ml min^{-1}) with water vapour was introduced into this system at this temperature for 30 min. Simultaneously, in situ thermal DRIFTS spectra were collected with the time stream on. The in situ photothermal DRIFTS spectra were measured similarly to the above operations but with Xe lamp irradiation.

Ultrafast IR spectroscopy. Briefly, UV–Vis pump/IR probe spectroscopy studies are performed with laser pulses (1 kHz, ~50 fs pulse width, 800 nm central wavelength) from an amplified Ti/sapphire laser system (Uptek Solutions) split into two parts. One is used to pump a femtosecond OPA (TOPAS-Prime) producing ~60 fs UV/Vis pulses with a bandwidth of ~10 nm in a tunable frequency range from 250 nm to 800 nm with ~2 mW at 1 kHz. The other is used to pump another femtosecond OPA (Palitra, QUANTRONIX) producing mid-IR pulses with a bandwidth ~200 cm^{-1} in a tunable frequency ranging from 1,000 cm^{-1} to 3,500 $cm^{-1}$with energy ~1 mW at 1 kHz. The mid-IR pulse is used as the probe beam and collected by 2 × 64 pixel mercury cadmium telluride detector (Infrared Associates). Two polarizers are inserted into the mid-IR beam pathway: one is located behind the sample to selectively measure the parallel or vertical polarized signal relative to the pump beam, and another is before the sample, which is used to rotate the polarization of the probe beam 45° relative to that of the pump beam. Measuring the transmission of the mid-IR beam through the sample by chopping the pump beam at 500 Hz, the pump–probe signal $P(t)$ is collected and the vibrational lifetimes are obtained from the rotation-free signal $P(t) = (P_{\parallel}(t) + 2P_{\perp}(t))/3$, and anisotropy is calculated from the following equation:

$$P(t) = (P_{\parallel}(t) - P_{\perp}(t))/(P_{\parallel}(t) + 2P_{\perp}(t)), \quad (1)$$

where $P_{\parallel}(t)$ and $P_{\perp}(t)$ are parallel and vertical signals, respectively.

For in situ ultrafast IR of the TiO_{2-x}/Ni-450 catalyst under reaction conditions, the reduced sample was firstly pressed into the sheet and loaded into a reactor cell, followed by 50 ml min^{-1} CO (CO/Ar = 96/4) with water vapour flow into the reactor cell for 1 h under atmospheric conditions. Then, the non-mobile system was formed by closing the valve. Simultaneously, in situ ultrafast IR spectra were collected with the pump on.

Catalytic tests

The reaction was carried out using a 300 W Xe lamp as the light source without adding external heating during the reaction. The photothermal catalytic reactor was approximately 69 ml stainless steel container and has a quartz window that can transmit light. For each test, 50 mg of the catalyst was placed in the reactor, and then the reactor was purged with reaction gas (CO/Ar = 96/4) for 30 min at a rate of 60 ml min^{-1}. Meanwhile, the 100 µl H_2O in liquid was imported into the reactor by syringe. During the reaction process, the temperature of the reactor will arise due to the Xe lamp irradiation, and the liquid water will turn into water vapour and participate in the reaction. The non-mobile system was formed by closing the valve. After each reaction, the gas-phase products were analysed by an Agilent 7820A equipped with a thermal conductivity detector and a flame ionization detector. Porapark Q and a 5 Å molecular sieve packed column were connected to a thermal conductivity detector to detect permanent gases, including H_2, CO_2,

CO, CH_4 and Ar, while an Al_2O_3 capillary column was connected to an flame ionization detector to analyse gaseous C_1–C_7 hydrocarbons. CO conversion was defined as follows:

$$\text{CO conversion}\ (\%) = \frac{F_{\text{CO,in}} - F_{\text{CO,out}}}{F_{\text{CO,in}}} \times 100. \quad (2)$$

Product selectivity was defined as follows:

$$\text{Selectivity}\ (\text{mol}\%) = \frac{F_{\text{C}i} \times i}{F_{\text{CO,in}} - F_{\text{CO,out}}} \times 100, \quad (3)$$

where F is the moles of CO and product Ci (CO_2 and hydrocarbon) containing i carbon atoms.

DFT calculations

All spin-polarized DFT calculations were performed by using the Vienna Ab initio Simulation Package (VASP)[36,37]. The p(2 × 2) slab model was used to model the Ni(111) surface allowing the topmost two Ni metal layers to relax. The interfacial TiO_{2-x}/Ni catalyst was modelled by using a three-layered Ni ribbon, consisting of three columns of Ni atoms, adsorbed on the two-layer p(4 × 2) TiO_2(101) surface. The Ni ribbon and the topmost TiO_2 layer were allowed to relax for the TiO_{2-x}/Ni surface calculations. Monkhorst–Pack **k**-point grids of 6 × 6 × 1 and 1 × 1 × 1 were used for Ni(111) and TiO_{2-x}/Ni surface calculations, respectively. A vacuum layer of 15 Å was employed to prevent spurious interactions between the repeated slabs. The improved force reversal method[38] was used to locate the transition states with a force tolerance of 0.05 eV $Å^{-1}$. Some transition states were verified using the climbing-image nudged elastic band method[39,40] and confirmed by vibrational frequency analysis. The zero-point energy correction was not taken into account in the present work. The activation barrier was computed as the energy difference between the transition state and initial state. An extra electron was added to TiO_{2-x}/Ni surface to model the photo-excited TiO_{2-x}/Ni catalyst based on the experimental finding that more photoinduced electrons can transfer from TiO_{2-x} to the Ni surface. This approach is widely and successfully used to model the charge distribution close to the interface of the catalyst during photocatalysis[41–44]. Two more extra electrons were introduced into the TiO_{2-x}/Ni catalyst and the entropy effect imposed by temperature only change the activation barriers within 0.08 eV and do not influence our conclusion (Supplementary Figs. 29 and 30). All the possible adsorption configurations of intermediates and reaction pathways of CO hydrogenation towards CH_4/C_2H_4 were fully considered on Ni(111) and TiO_{2-x}/Ni surfaces (Supplementary Figs. 31 and 40). The most favourable adsorption configurations and reaction mechanism for CO hydrogenation towards CH_4/C_2H_4 following the lowest energy reaction coordinate on the Ni(111) surface and at the interface of the TiO_{2-x}/Ni catalyst are shown and discussed in the present work. All the energetics were calculated with respect to the reactants at infinite separation over all the considered surfaces, except with respect to the co-adsorbed reactants over the photo-excited TiO_{2-x}/Ni surface. More calculation details can be found in Supplementary Information.

Data availability

The authors declare that all data supporting the findings of this study are available within the paper and Supplementary Information files. Source data are provided with this paper.

References

1. Rommens, K. T. et al. Molecular views on Fischer–Tropsch synthesis. *Chem. Rev.* **123**, 5798–5858 (2023).
2. Lin, T. et al. Advances in selectivity control for Fischer–Tropsch synthesis to fuels and chemicals with high carbon efficiency. *ACS Catal.* **12**, 12092–12112 (2022).
3. *Air Quality Guidelines—Second Edition* (US Environmental Protection Agency, Office of Research and Development, 2000).
4. *Air Quality Criteria for Carbon Monoxide, Publication No. EPA 600/P-99/001F* (US Environmental Protection Agency, Office of Research and Development, 2000).
5. Torres Galvis, H. M. & de Jong, K. P. Catalysts for production of lower olefins from synthesis gas: a review. *ACS Catal.* **3**, 2130–2149 (2013).
6. Yang, C. et al. Construction of synergistic Fe_5C_2/Co hetero-structured nanoparticles as an enhanced low temperature Fischer–Tropsch synthesis catalyst. *ACS Catal.* **7**, 5661–5667 (2017).
7. Kölbel, H., Ackermann, P., Ruschenburg, E., Langheim, R. & Engelhardt, F. Beitrag zur Fischer–Tropsch-Synthese an Eisen-Kontakten (Teil I). *Chem. Ing. Tech.* **23**, 153–157 (1951).
8. Zhang, X. et al. A stable low-temperature H_2-production catalyst by crowding Pt on alpha-MoC. *Nature* **589**, 396–401 (2021).
9. Yao, S. et al. Atomic-layered Au clusters on alpha-MoC as catalysts for the low-temperature water-gas shift reaction. *Science* **357**, 389–393 (2017).
10. Xu, M. et al. Insights into interfacial synergistic catalysis over Ni@TiO_{2-x} catalyst toward water–gas shift reaction. *J. Am. Chem. Soc.* **140**, 11241–11251 (2018).
11. Lin, L. et al. Heterogeneous catalysis in water. *JACS Au* **1**, 1834–1848 (2021).
12. Smith, A. et al. Hydrocarbon formation from metal carbonyl clusters supported on highly divided oxides. *JACS* **100**, 2590–2591 (1978).
13. Larkins, F. P. & Khan, A. Z. Investigation of Kölbel–Engelhardt synthesis over iron-based catalysts. *Appl. Catal.* **47**, 209–227 (1989).
14. Xu, Y. et al. Direct conversion of CO and H_2O into liquid fuels under mild conditions. *Nat. Commun.* **10**, 1389 (2019).
15. Zhao, Y. et al. Oxide-modified nickel photocatalysts for the production of hydrocarbons in visible light. *Angew. Chem. Int. Ed. Engl.* **55**, 4215–4219 (2016).
16. Zhao, Y. et al. Reductive transformation of layered-double-hydroxide nanosheets to Fe-based heterostructures for efficient visible-light photocatalytic hydrogenation of CO. *Adv. Mater.* **30**, e1803127 (2018).
17. Zhao, L. et al. Solar-driven water–gas shift reaction over CuO_x/Al_2O_3 with 1.1% of light-to-energy storage. *Angew. Chem. Int. Ed. Engl.* **58**, 7708–7712 (2019).
18. Liu, F. et al. Cu-based mixed metal oxides for an efficient photothermal catalysis of the water–gas shift reaction. *Catal. Sci. Technol.* **9**, 2125–2131 (2019).
19. Tong, Y. et al. Photocarriers-enhanced photothermocatalysis of water-gas shift reaction under H_2-rich and low-temperature condition over CeO_2/$Cu_{1.5}Mn_{1.5}O_4$ catalyst. *Appl Catal. B* **298**, 120551 (2021).
20. Xu, M. et al. TiO_{2-x}-modified Ni nanocatalyst with tunable metal–support interaction for water–gas shift reaction. *ACS Catal.* **7**, 7600–7609 (2017).
21. Chaffee, A. L. & Loeh, H. J. The Kölbel–Engelhardt reaction over a silica supported nickel catalyst. Variation of product distributions with reaction conditions. *Appl. Catal.* **26**, 123–139 (1986).
22. Vannice, M. Metal–support effects on the activity and selectivity of Ni catalysts in CO/H_2 synthesis reactions. *J. Catal.* **56**, 236–248 (1979).
23. Hernández Mejía, C., Vogt, C., Weckhuysen, B. M. & de Jong, K. P. Stable niobia-supported nickel catalysts for the hydrogenation of carbon monoxide to hydrocarbons. *Catal. Today* **343**, 56–62 (2020).
24. Ghoussoub, M., Xia, M., Duchesne, P. N., Segal, D. & Ozin, G. Principles of photothermal gas-phase heterogeneous CO_2 catalysis. *Energy Environ. Sci.* **12**, 1122–1142 (2019).

25. Xie, J. et al. Highly selective oxidation of methane to methanol at ambient conditions by titanium dioxide-supported iron species. *Nat. Catal.* **1**, 889–896 (2018).
26. Kazansky, V. B. & Pidko, E. A. Intensities of IR stretching bands as a criterion of polarization and initial chemical activation of adsorbed molecules in acid catalysis. Ethane adsorption and dehydrogenation by zinc ions in ZnZSM-5 zeolite. *J. Phys. Chem. B* **109**, 2103–2108 (2005).
27. Wang, F. et al. Active site dependent reaction mechanism over Ru/CeO_2 catalyst toward CO_2 methanation. *J. Am. Chem. Soc.* **138**, 6298–6305 (2016).
28. Zhang, Y. et al. Tuning reactivity of Fischer–Tropsch synthesis by regulating TiO_x overlayer over Ru/TiO_2 nanocatalysts. *Nat. Commun.* **11**, 3185 (2020).
29. Iyer, V. et al. Infrared ultrafast spectroscopy of solution-grown thin film tellurium. *Phys. Rev. B* **100**, 075436 (2019).
30. Zhou, P. & Han, K. Unraveling the detailed mechanism of excited-state proton transfer. *Acc. Chem. Res.* **51**, 1681–1690 (2018).
31. Pensack, R. D., Banyas, K. M., Barbour, L. W., Hegadorn, M. & Asbury, J. B. Ultrafast vibrational spectroscopy of charge-carrier dynamics in organic photovoltaic materials. *Phys. Chem. Chem. Phys.* **11**, 2575–2591 (2009).
32. Tamaki, Y. et al. Trapping dynamics of electrons and holes in a nanocrystalline TiO_2 film revealed by femtosecond visible/near-infrared transient absorption spectroscopy. *C. R. Chim.* **9**, 268–274 (2006).
33. Pensack, R. D. & Asbury, J. B. Barrierless free carrier formation in an organic photovoltaic material measured with ultrafast vibrational spectroscopy. *J. Am. Chem. Soc.* **131**, 15986–15987 (2009).
34. Xu, M. et al. Boosting CO hydrogenation towards C_{2+} hydrocarbons over interfacial TiO_{2-x}/Ni catalysts. *Nat. Commun.* **13**, 6720 (2022).
35. van Santen, R. A., Markvoort, A. J., Filot, I. A., Ghouri, M. M. & Hensen, E. J. Mechanism and microkinetics of the Fischer–Tropsch reaction. *Phys. Chem. Chem. Phys.* **15**, 17038–17063 (2013).
36. Kresse, G. & Hafner, J. Ab initio molecular dynamics for liquid metals. *Phys. Rev. B* **47**, 558–561 (1993).
37. Kresse, G. & Furthmüller, J. Efficient iterative schemes for ab initio total-energy calculations using a plane-wave basis set. *Phys. Rev. B* **54**, 11169–11186 (1996).
38. Sun, K., Zhao, Y., Su, H. Y. & Li, W. X. Force reversed method for locating transition states. *Theor. Chem. Acc.* **131**, 1118 (2012).
39. Henkelman, G., Uberuaga, B. P. & Jónsson, H. A climbing image nudged elastic band method for finding saddle points and minimum energy paths. *J. Chem. Phys.* **113**, 9901–9904 (2000).
40. Henkelman, G. & Jónsson, H. Improved tangent estimate in the nudged elastic band method for finding minimum energy paths and saddle points. *J. Chem. Phys.* **113**, 9978–9985 (2000).
41. Huang, P.-R. et al. Impact of lattice distortion and electron doping on α-MoO_3 electronic structure. *Sci. Rep.* **4**, 7131 (2014).
42. Chan, M. K. Y. & Ceder, G. Efficient band gap prediction for solids. *Phys. Rev. Lett.* **105**, 196403 (2010).
43. Li, Y.-F. et al. Adsorption and reactions of O_2 on anatase TiO_2. *Acc. Chem. Res.* **47**, 3361–3368 (2014).
44. Xu, S. & Carter, E. A. Theoretical insights into heterogeneous (photo)electrochemical CO_2 reduction. *Chem. Rev.* **119**, 6631–6669 (2019).

Acknowledgements

This work was supported by the National Key R&D Program of China (2022YFE0114900, 2021YFB3800300, 2021YFA1500303, 2021YFA1500300 and 2021YFA1502804), the National Natural Science Foundation of China (NSFC: 22102007, 21991150, 22222306, 22172150, 21821004 and 22072090), the Fundamental Research Funds for the Central Universities (buctrc202112), Certificate of China Postdoctoral Science Foundation Grant (2019M650306 and 2020T130010), USTC Research Funds of the Double First-Class Initiative (YD2060002012), K. C. Wong Education (GJTD-2020-15), Science and Technology Program of Sichuan Province (2021YFSY0021), Innovation Program for Quantum Science and Technology (2021ZD0303302), and the New Cornerstone Science Foundation. We thank the support of the BSRF (Beijing Synchrotron Radiation Facility) during the XAFS measurements at beamline 1W1B. We also appreciate technical support from H. Matsumoto and C. Zeng, Hitachi High-Technologies (Shanghai) Co. Ltd, for high-resolution STEM characterization. High-performance computational resources were provided by the University of Science and Technology of China and Hefei Advanced Computing Center. D.M. acknowledges support from the Tencent Foundation through the XPLORER PRIZE.

Author contributions

D.M. designed the study. X.Q., M.X. and R.Z. conducted material synthesis and carried out the catalytic performance test. X.Q. carried out the in situ DRIFTS experiment and data analysis. X.Q. and J. Zhang carried out the CO chemisorption experiment. X.Q., J.G., J. Zheng., Z.Y. and X. Li carried out the in situ ultrafast IR experiment and data analysis. X.Q., M.X. and L.Z. conducted the X-ray absorption fine structure spectroscopy measurements and analysed the data. Y.X. and J.X. carried out quasi in situ XPS experiments and data analysis. X. Liu contributed to the measurement and analysis of the environmental STEM experiment. J.-X.L., L.F., J.-W.Z. and J.-L.C. performed the DFT calculations. X.Q., M.X., J.G., J.-X.L., X. Liu, M.W. and D.M. wrote the paper. All authors performed certain experiments and discussed and revised the paper.

Competing interests

The authors declare no competing interests.

Additional information

Supplementary information The online version contains supplementary material available at https://doi.org/10.1038/s41560-023-01418-1.

Correspondence and requests for materials should be addressed to Xi Liu, Jin-Xun Liu, Junrong Zheng or Ding Ma.

Peer review information *Nature Energy* thanks Shuxin Ouyang, Yuan Ping, Lianzhou Wang and the other, anonymous, reviewer(s) for their contribution to the peer review of this work.